Nuclear Engineering and Technology 53 (2021) 1909–1923

Contents lists available at ScienceDirect

Nuclear Engineering and Technology

journal homepage: www.elsevier.com/locate/net

Original Article

Development of probabilistic primary water stress corrosion cracking initiation model for alloy 182 welds considering thermal aging and cold work effects

Jae Phil Park [a], Seung Chang Yoo [b], Ji Hyun Kim [b, **], Chi Bum Bahn [a, *]

[a] School of Mechanical Engineering, Pusan National University, Busan, 46241, Republic of Korea
[b] School of Mechanical, Aerospace and Nuclear Engineering, Ulsan National Institute of Science and Technology, Ulsan, 44919, Republic of Korea

ARTICLE INFO

Article history:
Received 23 September 2020
Received in revised form
26 November 2020
Accepted 6 December 2020
Available online 10 December 2020

Keywords:
PWSCC Initiation
Thermal aging
Cold rolling
Probabilistic model

ABSTRACT

We experimentally investigated the effects of thermal aging and cold work on the microstructure, mechanical properties, and primary water stress corrosion cracking (PWSCC) initiation time for Alloy 182 welds. The effects of thermal aging and cold work on the PWSCC initiation time of Alloy 182 were modeled based on the plastic energy concept and the PWSCC initiation data of this study and previous reports by considering censored data. Based on the results, it is estimated that the PWSCC resistance of the Alloy 182 weld firstly increases and then decreases with thermal aging time when the applied stress is kept constant.

1. Introduction

Over the past few decades, the initiation of primary water stress corrosion cracking (PWSCC) in the pressure boundary components composed of Ni-based alloys (e.g., Alloy 600/182) has been one of the most critical safety issues, threatening the structural integrity of nuclear power plants (NPPs) [1–5]. Therefore, it is crucial to predict the initiation of PWSCC under a given condition of components. In particular, such predictions are more important in the case of Alloy 182 welds than the Alloy 600 base metal, because the reported crack growth rate of the former is approximately five times higher than that of the latter [4]. In addition, some laboratory tests have reported that the PWSCC susceptibility of Alloy 182 is greater than that of Alloy 600 [6–9].

However, although numerous studies have been conducted to study the PWSCC of Ni-based alloys, a physical formula for accurately predicting PWSCC initiation time considering the many affecting factors and complexity of the PWSCC phenomenon has not been proposed thus far. Therefore, most probabilistic fracture mechanics (PFM) code (e.g., PRAISE [10], PRO-LOCA [11]) used empirical crack initiation models as a module in the code. In particular, the most recent PFM code, called *eXtremely Low Probability of Rupture* (xLPR), developed for regulatory purposes by the Nuclear Regulatory Commission and Electric Power Research Institute [12–14], adopted the following two empirical models for the PWSCC initiation in Alloy 182 welds: 1) *the stress–power model* and 2) *the Garud model*.

The stress–power model describes the PWSCC initiation time as a function of stress and temperature, as follows [4,9,12,14]:

$$t_i \propto \sigma^{-n} . e^{Q/RT} \tag{1}$$

where t_i is the PWSCC initiation time, σ is the applied true stress, n is the stress exponent, Q is the activation energy of PWSCC initiation, R is the universal gas constant, and T is the absolute temperature. As shown in Eq. (1), the stress–power model is proportional to the stress–power term and the Arrhenius-type temperature effect term. Amzallag et al. suggested an activation energy of 185 kJ/mol for Alloy 182 with the applicable temperature ranging from 330 °C to 360 °C [9,15]. Troyer et al. suggested the value of 5 for the stress exponent using published laboratory PWSCC initiation data on Alloys 82/182/132 welds [14]. However, it should be noted that Troyer et al. did not consider right-censored data (i.e., no cracking or suspension). Furthermore, the estimated stress exponents for

* Corresponding author.
** Corresponding author.
E-mail addresses: kimjh@unist.ac.kr (J.H. Kim), bahn@pusan.ac.kr (C.B. Bahn).

https://doi.org/10.1016/j.net.2020.12.005

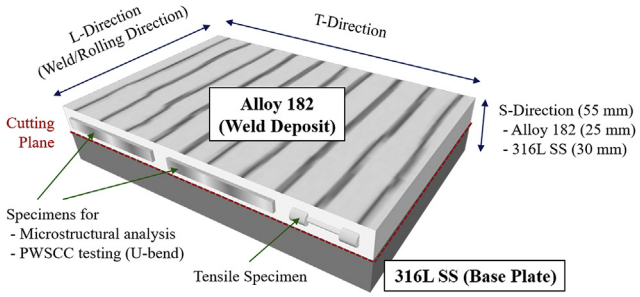

Fig. 1. Schematic of Alloy 182 weld deposit and direction of specimens.

each individual data set in Ref. [14] varied widely from 1.8 to 8.3, and the suggested value of 5 for the stress exponent was determined only based on engineering judgements.

The Garud model is more complicated and describes the PWSCC initiation time as a function of stress, mechanical properties, and temperature, as follows [12,14,16,17]:

$$t_i \propto \ln(A)\frac{\ln\left(\frac{A-z}{\frac{\sigma}{YS_{RT}}-z}\right)}{\ln\left(\frac{A-z}{1-z}\right)}\frac{1}{m^q}.e^{Q/RT} \tag{2a}$$

where

$$m = k\left(\frac{YS_{RT}}{E_{RT}}\right)^a (r-1)^b (r)^c \tag{2b}$$

$$A = v\exp[wr] \tag{2c}$$

$$z = z_1 + z_2 \ln r \tag{2d}$$

$$r = \frac{UTS_{RT}}{YS_{RT}} \tag{2e}$$

YS_{RT}, UTS_{RT} and E_{RT} are the yield strength (YS), ultimate tensile strength (UTS), and elastic modulus at room temperature (RT), respectively. In particular, the ratio of applied stress to YS at RT (i.e., σ/YS_{RT}) is called *stress severity* [16]. m is the measure of cold work; A is the microcracking resistance (or upper limit of stress severity); z is the PWSCC threshold (or lower limit of stress severity); r is the strength ratio; and a, b, c, k, v, w, q, z_1, and z_2 are the fitting parameters. Compared to the stress–power model, the Garud model has an advantage in that it considers the mechanical properties of the material; therefore, the effects of heat treatment or cold work can be reflected. However, the model parameters suggested by Garud [16] were validated for Alloy 600 and not for Alloy 182 welds. Considering residual stress and microstructural differences at the weld, it is anticipated that Alloy 182 welds would have somewhat different parameters in the Garud model.

Owing to the long-term operation of existing NPPs, it is important to consider the effect of thermal aging on PWSCC initiation. Generally, Alloy 600/182 are known to be non-age-hardening materials by the intermetallic γ' phase [18,19]. However, during long-term thermal aging, it has been reported that the incoherent precipitates such as Cr carbides that have relatively high interfacial energy can nucleate and grow [20]. In regard to this, some studies have reported that the microstructure and mechanical properties of Ni-based alloys can be changed when subjected to thermal aging [20–25]. Regarding the effect of thermal aging on the PWSCC initiation resistance, Yoo et al. [20] reported that the PWSCC resistance could decrease and increase depending on thermal aging time of Alloy 600; however, there is no such associated research for Alloy 182 welds.

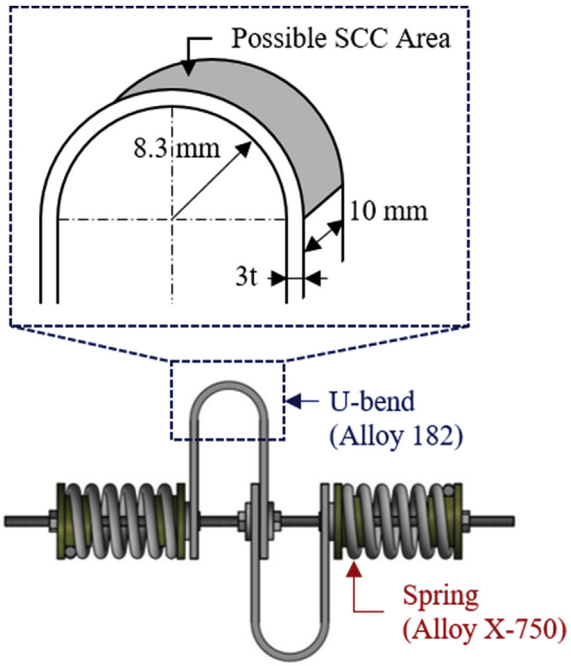

Fig. 2. Schematic of U-bend specimen for PWSCC initiation test.

Cold working is another process that can significantly alter the mechanical properties, microstructures, and PWSCC resistance of Ni-based alloys [26,27]. It is widely known that it decreases the PWSCC resistance of such materials. Cold work can be performed during metal processing or intentionally implemented in testing specimens in order to accelerate PWSCC initiation tests [28]. Thus, it is also important to appropriately model the cold work effects with respect to the PWSCC initiation time. As mentioned earlier, the Garud model considers the effect of cold work; however, it still needs to be calibrated for Alloy 182 welds.

In this context, we experimentally investigated the effects of thermal aging and cold work on the microstructure, mechanical properties, and PWSCC initiation of Alloy 182 welds. In addition, to develop a PWSCC initiation model for Alloy 182 considering the effects of thermal aging and cold work, we adopted a two-track approach as follows: 1) parameters of the Garud model were calibrated for Alloy 182, and 2) a new PWSCC initiation model based on the plastic energy concept was developed. The PWSCC initiation data used for the model development included not only the experimental data from this work but also data from published reports considering right-censored data.

Table 1
Chemical composition of Alloy 182.

Element	C	Si	Mn	P	S	Fe	Cu	Ni	Ti	Cr	Nb + Ta
w.t.%	0.048	0.08	8.38	0.011	0.007	3.10	0.01	73.08	0.02	13.97	1.29

Table 2
Information of PWSCC initiation test specimens.

Specimen		Number of Specimens (ea.)	Specimen Index
Designation	Condition		
AW	No post processing, as-welded	16	#1 - #6[a] #7 - #16
15Y	Thermally aged for time equivalent to 15 years	10	#17 - #26
30Y	Thermally aged for time equivalent to 15 years	10	#27 - #36
CR	Cold rolled with 20% thickness reduction	10	#37 - #46

[a] Specimens from #1 to #6 were initially tested at 325 °C up to 1200 h and additionally tested at 340 °C until cracking.

2. Experimental methods

2.1. Preparation of test specimens

The Alloy 182 weld deposit was prepared on a 316 L stainless steel (SS) plate using shielded metal arc welding (see Fig. 1). The welding current, voltage, and speed ranges were 140–150 A, 25–28 V, and 15–18 cm/min, respectively. Table 1 shows the chemical composition of the Alloy 182 weld. After welding, the fabricated weld deposit was divided into four parts to assign different post-processing as follows:

1) No post-processing, as-welded (AW)
2) Heat treatment equivalent to 15 years of thermal aging during plant operation (15Y)
3) Heat treatment equivalent to 30 years of thermal aging during plant operation (30Y)
4) Cold work via cold rolling with 20% thickness reduction (CR)

The plant operation temperature was assumed to be 320 °C. To simulate the 15Y and 30Y thermal aging conditions, we conducted accelerated heat treatment at 400 °C under an argon environment for 1713 h and 3427 h, respectively. The heat treatment temperature of 400 °C was obtained using thermodynamic calculations, which is the highest temperature to avoid sigma phase or precipitates that could be formed above 450 °C [20]. The heat treatment durations were determined using the following modified Arrhenius equation [20]:

$$\frac{t_{HT}}{t_{plant}} = \exp\left[-\frac{Q_{TA}\left(\frac{1}{T_{plant}} - \frac{1}{T_{HT}}\right)}{R}\right] \quad (3)$$

where t_{HT} and T_{HT} are the heat treatment time and temperature and t_{plant} and T_{plant} are the intended plant operation time and temperature for simulation, respectively; R is the universal gas constant, and Q_{TA} is the activation energy of thermal aging. It has been previously reported that Cr strongly affects corrosion and PWSCC resistance [29]; thus, the activation energy Q_{TA} is assumed to be 180 kJ/mol, which corresponds to the Cr diffusion energy along the grain boundary within the temperature range of interest [20,30].

For cold work processing (i.e., CR condition), five steps of cold rolling were carried out to achieve a thickness reduction of 20% after cutting the Alloy 182 portion from the 316-L SS base plate along the cutting plane (red line in Fig. 1). After post-processing, specimens for microstructural analyses and the tensile and PWSCC tests were cut using electrical discharge machining along the T-L direction, as illustrated in Fig. 1; this approach was employed because previous reports indicate that the T-L direction is most susceptible to PWSCC [31].

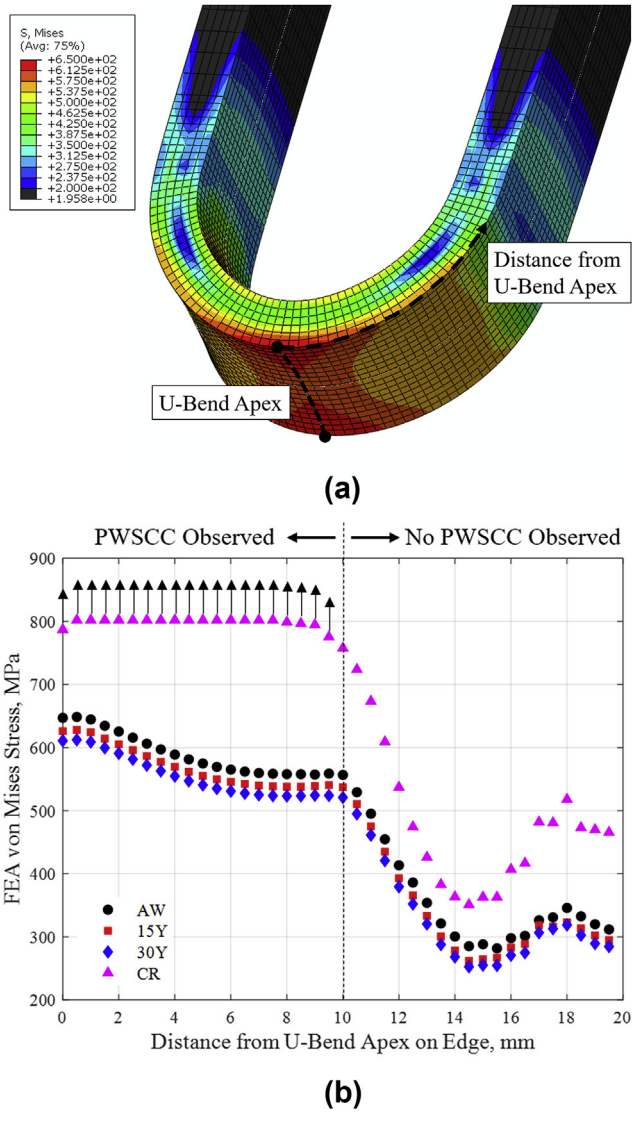

Fig. 3. Result of U-bend stress estimation by FEA, (a) von Mises stress distribution of AW specimen surface and (b) comparison of von Mises stresses as function of distance from U-bend apex.

2.2. Microstructural analysis

The specimens for the microstructural analysis were ground using SiC papers up to 800 grit and polished with diamond pastes and colloidal silica up to 0.02 μm. Subsequently, vibratory polishing was applied with 0.02 μm of colloidal silica solution for 1 h to minimize further mechanical deformation that could occur during

Table 3
Measured mechanical properties from tensile test (mean ± standard deviation).

Specimen Condition		CR	AW	15Y	30Y
0.2% Offset Yield Strength (YS) [MPa]	RT	711.8 ± 49.7	425.0 ± 4.97	421.7 ± 11.5	412.9 ± 10.1
	325 °C	628.8 ± 25.6	370.7 ± 10.9	347.1 ± 12.4	321.9 ± 13.7
Ultimate Tensile Strength (UTS) [MPa]	RT	795.9 ± 12.9	603.2 ± 26.4	631.1 ± 14.3	636.0 ± 9.63
	325 °C	724.5 ± 21.7	561.8 ± 6.17	554.7 ± 7.29	530.8 ± 11.5
Uniform Elongation (uEL) [%]	RT	8.00 ± 1.21	27.61 ± 5.44	34.99 ± 1.89	39.23 ± 3.64
	325 °C	10.23 ± 1.92	34.43 ± 3.50	37.08 ± 3.55	34.63 ± 3.17
Total Elongation (tEL) [%]	RT	14.36 ± 2.13	30.99 ± 7.24	40.31 ± 2.05	44.93 ± 4.13
	325 °C	14.93 ± 2.44	38.78 ± 2.84	42.42 ± 4.75	38.71 ± 3.23

mechanical polishing. To reveal general microstructures, specimens were etched using 20% of HCl + HNO_3 solution for 3 min, according to the ASTM E407-07 standard [32]. Thereafter, microstructural characterization was conducted using an optical microscope (OM) and the Quanta 3D dual-beam focused ion beam (FIB) attached to a field-emission gun scanning electron microscope (SEM). For a more detailed investigation of the microstructural characteristics of the precipitates, transmission electron microscopy (TEM) analysis was conducted using JEOL JEM-2100F with a specimen prepared using FIB processing. The crystallographic orientations were investigated by conducting electron backscattered diffraction (EBSD) using SUPRA 40VP with an acceleration voltage of 20 kV, a tilt angle of 70°, a working distance of 15 mm, and a step size of 1.2 μm. The resulting EBSD data were analyzed using the open-source software toolbox MTEX [33].

2.3. Tensile test

The tensile tests were performed according to the ASTM E8/E8M standard [34] at both RT and 325 °C. During these tests, the tensile displacement rate was constantly maintained at 0.63 mm/min. A total of 45 specimens were fabricated following the standard rod-type design in the ASTM E8/E8M; however, the specimen size was proportionally reduced because of the limited size of the weld deposit.

2.4. PWSCC initiation test

The size of the as-machined PWSCC testing specimen was 10 mm × 100 mm × 3 mm. The PWSCC specimens were ground and polished following the same procedure used for the microstructural analysis, excluding the final vibratory polishing and etching processes. Subsequently, the specimens were deformed to have a U-bend shape, according to the ASTM G30 standard [35]. Fig. 2 illustrates the schematic of the fabricated U-bend specimens. The specimens were loaded and constrained using the Inconel alloy X-750 high-strength spring to mitigate stress relaxation at the elevated testing temperature. Other components that could contact the Alloy 182 U-bend were composed of Alloy 600 to prevent galvanic corrosion. A total of 46 U-bend specimens were fabricated and tested (see Table 2) under the simulated primary water condition of the pressurized water reactor (PWR) with the testing temperature of 340 °C, autoclave pressure of 16 MPa, dissolved oxygen of less than 5 ppb, dissolved hydrogen of 30 cc/kg H_2O, and Li and B concentrations of 1200 ppm and 2 ppm, respectively.

During the PWSCC test, the U-bend specimens were periodically retrieved from the autoclave to identify the occurrence of PWSCC. In this work, the criterion of crack initiation was whether or not a crack is visible through naked eyes. When cracks were first detected, the minimum crack length was around 2 mm. As shown in Table 2, specimens #1 to #6 were initially tested at 325 °C for

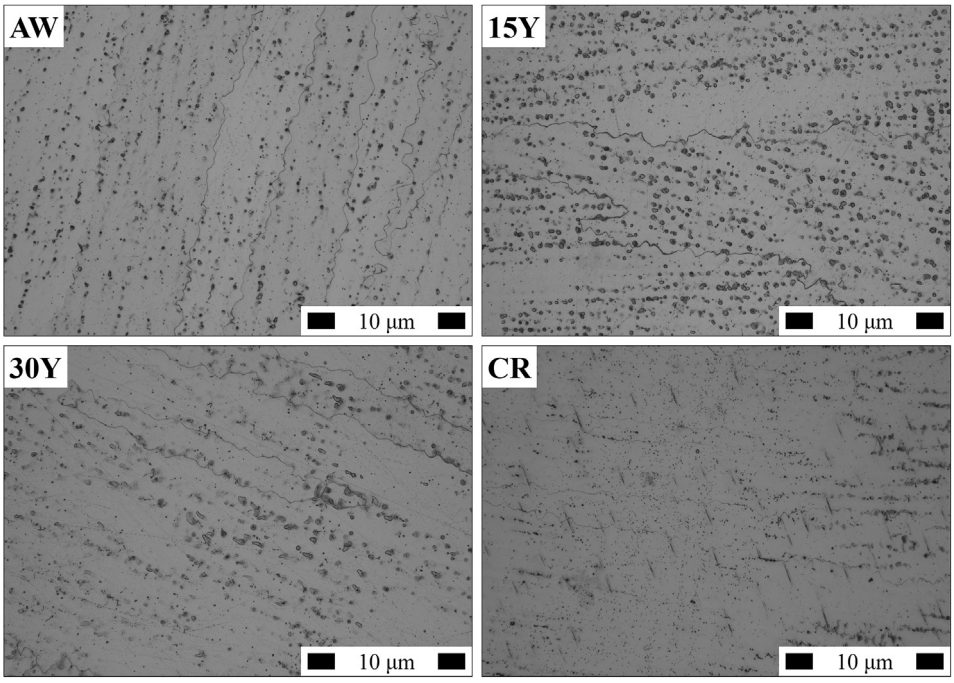

Fig. 4. Microstructure of Alloy 182 observed by OM.

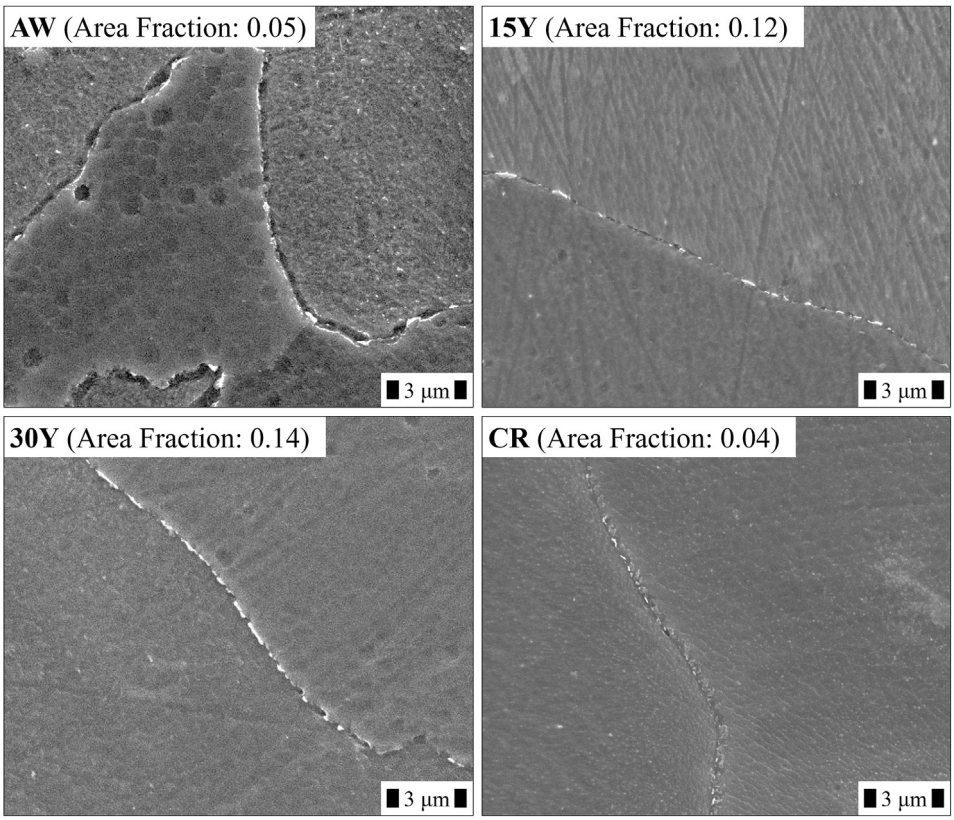

Fig. 5. Secondary electron SEM images of Alloy 182 weld focusing on grain boundary precipitates and estimated average area fraction (unit: %).

1200 h and then tested again at 340 °C until cracking. Therefore, we corrected the effect of different testing temperature for the initial 1200 h by using the Arrhenius equation with an activation energy of 185 kJ/mol [4,9,14].

For a more realistic estimate of the applied stress/strain in the U-bend specimens, a commercial finite element analysis (FEA) software ABAQUS (Ver. 2016) [36] was used. The input material properties for plastic stress–strain (S–S) data were obtained from the tensile test results (see Section 3.2). Other input properties such as elastic modulus, Poisson's ratio, and temperature-dependent thermal expansion coefficient were obtained from published data of Alloy 600 [37]. The FEA was conducted via the following two steps: 1) U-bending at room temperature using rigid rollers and 2) increasing the specimen temperature up to 325 °C. The difference between 325 °C (i.e., FEA temperature) and 340 °C (i.e., PWSCC test temperature) is minor; thus, we assumed that the estimated stress difference caused by this small temperature difference would be negligible. Detailed procedure of the FEA is described in the Supplementary Material.

Fig. 3 shows the estimation results of the U-bend stress via FEA. Because the applied stress in the U-bend specimen is not uniaxial, the von Mises effective stress is represented and used in this study. From Fig. 3 (a), it is evident that the estimated stress increases when the concerned location is close to the U-bend apex and edges. Fig. 3 (b) shows that the stress applied to the CR specimen is the highest and that to the 30Y specimen is the lowest. However, it should be noted that the plotted stress of the CR specimen is only the lower bound because the calculated equivalent plastic strain (i.e., PEEQ) during the FEA exceeded the measured uniform elongation (see Table 3). It can be observed from Fig. 3 (b) that a sharp decrease in stress is shown at approximately 10 mm from the U-bend apex. This FEA result is in good agreement with the experimental observation that the PWSCC was not initiated further than a distance of 10 mm from the U-bend apex in this study.

3. Results and discussion

3.1. Microstructural analysis

First, we conducted microstructural analyses using an OM. As shown in Fig. 4, typical dendritic microstructures and solidification boundaries were observed. The average size of the grains was approximately 100 μm, although high anisotropy and irregular grain shapes were noted. The overall size of the grains did not change significantly due to thermal aging because the heat treatment temperature of 400 °C was insufficient to increase grain sizes. In the CR specimens, wedge-shaped defects were observed as a result of the dislocation concentrated around precipitates during cold rolling [38].

We focused on the precipitates along grain boundaries because the PWSCC in Alloy 182 welds is an intergranular phenomenon [8]. Fig. 5 shows the resulting SEM images and the estimated average precipitate area fraction. Multiple regions were analyzed to calculate the average area fraction of the precipitates. The area fraction shown in Fig. 5 was calculated using the image analysis software ImageJ [39]. The SEM images shown in Fig. 5 are only the representative images of all analyzed images. For each specimen, we analyzed about twenty images to estimate the area fraction which covers at least 1000 μm^2. It was shown that the amount and size (i.e., area fraction) of the precipitates increased with thermal aging. However, cold work had no noticeable effect on the precipitate fraction. The precipitation behavior of Alloy 182 has also been

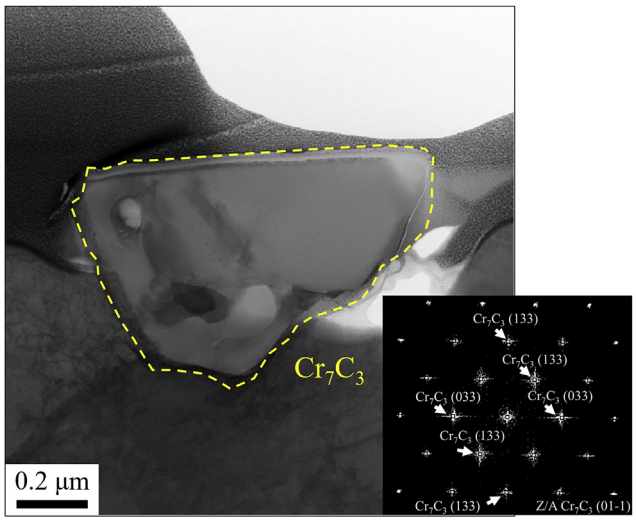

(a)

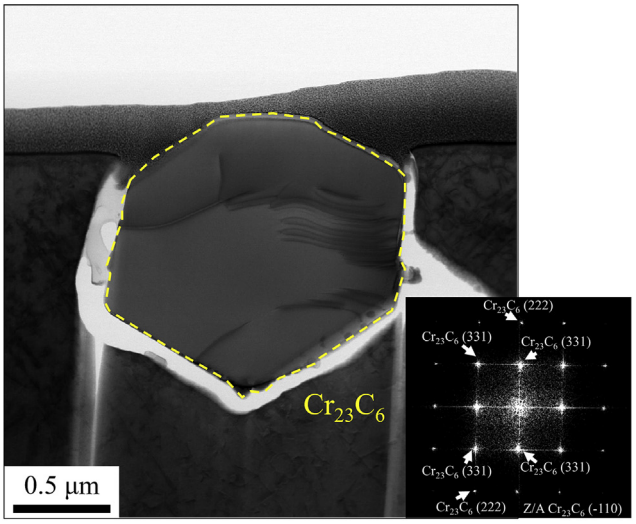

(b)

Fig. 6. Dark field TEM images and corresponding diffraction patterns of (a) Cr_7C_3 and (b) $Cr_{23}C_6$ precipitate along grain boundaries of Alloy 182 weld.

investigated by other researchers [40]. Various carbides such as NbC, $Cr_{23}C_6$, and Cr_7C_3 were observed, and Cr carbides formed and coarsened during heat treatment [41]. Fig. 6 shows the TEM images of the example grain boundary precipitates and their diffraction patterns. We found that the precipitates along grain boundaries were Cr carbides ($Cr_{23}C_6$ or Cr_7C_3), which is consistent with precedent research on similar materials [42–45]. The coarsened grain boundary precipitates, which were formed during thermal aging, were primarily composed of Cr carbides. This is apparent because the amount and diffusion rates of other minor elements (such as Nb and Ti) were relatively low at 400 °C. Therefore, it is confirmed that, as expected, sigma phases or precipitates were not formed due to thermal aging, with the exception of carbides.

Fig. 7 shows the first-order kernel average misorientation (KAM) images obtained from the EBSD analysis, which are closely related to the residual strain or dislocation density. For austenitic stainless steel, it has been reported that the average KAM value and measured true strain exhibit a linear relationship up to the true strain of 0.18 [46]. The average confidence indexes of all the images shown in Fig. 7 are above 0.72. The data were cleaned using the half-quadratic filter provided by the MTEX toolbox with the alpha value of 0.5 [47]. The values shown in Fig. 7 are the average KAM values estimated using each image shown in Fig. 7. It is clearly shown that cold work increases the value of KAM, in particular, near the grain boundaries, implying the accumulation of geometrically necessary dislocation [48]. On the contrary, thermal aging decreases the overall KAM value. Therefore, it is concluded that cold work increases localized residual strain and thermal aging relieves existing residual strain formed during the welding process.

Based on the microstructural analysis, it is apparent that the PWSCC susceptibility of the cold-rolled specimen is higher than that of the as-welded specimen due to the higher localized residual strain. However, the effect of thermal aging on the PWSCC susceptibility is slightly ambiguous. This is because there are both beneficial and detrimental effects caused by thermal aging. For example, thermal aging reduces existing residual strains (see Fig. 7) but it also reduces the elongation/toughness of the material (see Section 3.2). The effect of thermal aging on PWSCC initiation is discussed further in Section 3.3 along with the U-bend test results.

3.2. Tensile test

Fig. 8 shows the S– S curves of the Alloy 182 tensile specimens, and Table 3 summarizes the measured mechanical properties. At RT, it is shown that cold work increases both YS and UTS but decreases elongation. On the contrary, thermal aging increases UTS and elongation. At the elevated temperature of 325 °C, cold work increases both YS and UTS but decreases elongation, like the trend at RT. However, thermal aging decreases YS, UTS, and also elongation (30Y) at 325 °C, unlike the trend at RT.

At the concerned temperature of PWSCC initiation (i.e., 325 °C), it is likely that the material strength are dominantly affected by *work hardening* because there is a clear relationship between the material strength and the KAM. For example, CR specimen has the highest strength and KAM, and 30Y specimen has the lowest strength and KAM (see Fig. 7). Meanwhile, it is likely that the growth of precipitates through thermal aging has little effect on the material strength because those precipitates are intergranular. However, it should be noted that, especially at 30Y, the thermal aging reduces elongation of the material probably due to the coarsened intergranular precipitates. Lee et al. reported that the elongation of the Alloy 690 decreased with thermal aging because the coarsened intergranular Cr carbides caused the intergranular fracture during the tensile tests [49].

3.3. PWSCC initiation test

Fig. 9 shows the example images of PWSCC initiation and propagation. As shown in this figure, it was difficult to identify the occurrence of cracking until the crack was sufficiently wide because of the uneven specimen surface. The minimum length of the identifiable crack through the naked eyes was approximately 2 mm. It was observed that the average propagation speed of CR specimens was considerably higher than that of the other specimens. In other words, the PWSCC of the CR specimens was typically observed with a large crack spanning from one side to the other side of the U-bend edge at its first observation. Fig. 10 shows the example SEM images of the PWSCC fracture surface and cross

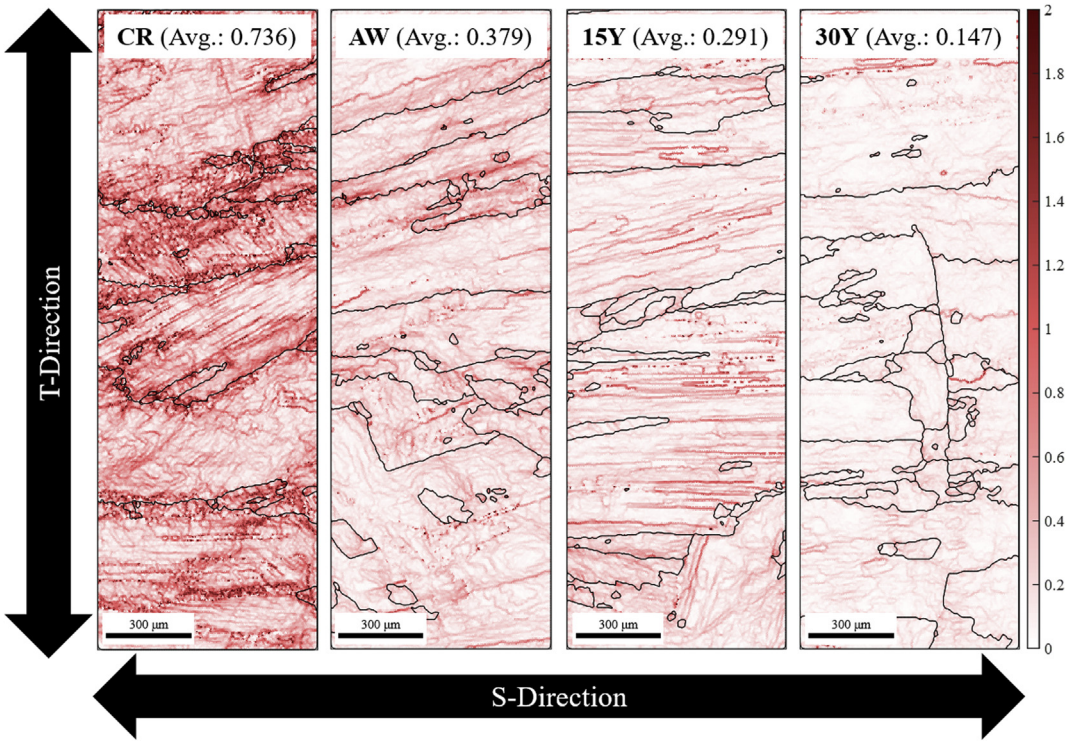

Fig. 7. First-order KAM images and average values of KAM for each image; color gradation indicates KAM (unit: °) and black lines are grain boundaries. (For interpretation of the references to color in this figure legend, the reader is referred to the Web version of this article.)

section. The observed fracture surfaces of PWSCC always appeared interdendritic [50,51], regardless of the post-processing conditions. We found some secondary and internal cracks in the CR specimens (see Fig. 10). This is likely due to the higher residual stress in the CR specimens.

Fig. 11 shows the result of the PWSCC initiation test with the U-bend specimens. Because of the large scattered and censored data (i.e., only the interval or lower limit is known for the PWSCC initiation time), a probabilistic approach was used. Thus, we first applied the 2-parameter Weibull distribution [52], which is widely used to model the lifetime of materials, as follows:

$$F(t;\beta,\eta) = 1 - \exp\left[-\left(\frac{t}{\eta}\right)^{\beta}\right] \tag{4}$$

where F is the cumulative distribution function (CDF), t is the time, and β and η are the shape and scale parameters of the Weibull distribution, respectively. The shape parameter β is related to the shape (or scatter) of the model. For example, if the value of β is infinity, the Weibull distribution becomes the deterministic model. The scale parameter η denotes the characteristic time (or life). It is the quantile at which the CDF of the Weibull distribution reaches approximately 0.632 ($\cong 1 - e^{-1}$). If $\beta = 1$, then η becomes the expectation of the Weibull distribution.

The abovementioned Weibull assumption is reasonable at least for macroscopic-scale failures governed by the *weakest link theory* [53,54]. To consider the censored data, we used the probabilistic method of maximum likelihood estimation (MLE) [54–57] to estimate parameters β and η of each specimen group. The objective of the MLE is to find a set of estimates that maximize the likelihood function for the given data. In this study, the estimates were numerically calculated using the *conjugate gradient* method [58]. The convergence criterion is when the L2 Norm of the relative difference becomes less than 10^{-6}. Table 4 shows the estimates, and Fig. 12 shows the resulting 2-parameter Weibull curve of each specimen. From the estimation result, it was shown that the estimates of the shape parameter $\hat{\beta}$ increased with thermal aging and decreased with cold work. Therefore, it was likely that the scatter of the PWSCC initiation time increased with the degree of localized residual strain (see the KAM analysis in Fig. 7). This result corresponds to the precedent research reporting a larger scatter of the SCC initiation time for Ni-based weld metals, as compared to that of the base metal [59,60].

In the case of the scale parameter estimates $\hat{\eta}$, which indicates the representative PWSCC initiation time, it was clearly shown that $\hat{\eta}$ decreased with cold work, as expected in Section 3.1. However, the effect of thermal aging on $\hat{\eta}$ was difficult to conclude because $\hat{\eta}$ increased at 15Y and then slightly decreased at 30Y, although the applied stress of the 30Y specimens was lower than that of the 15Y specimens [see Fig. 3 (b)]. Therefore, it is obvious that the microstructural change in the thermally-aged specimens plays an important role in the PWSCC resistance. This elucidates the limitation of the stress–power model (see Eq. (1)), which can only handle the applied stress effect on the PWSCC initiation time.

In this regard, the Garud model (see Eq. (2)) appears suitable for this case because it considers the mechanical properties of the material, which are the macroscopic results originated from microstructural changes such as dislocation density or precipitate size (see Section 3.2). In addition, the PWSCC initiation model based on mechanical properties is more convenient to use than the model

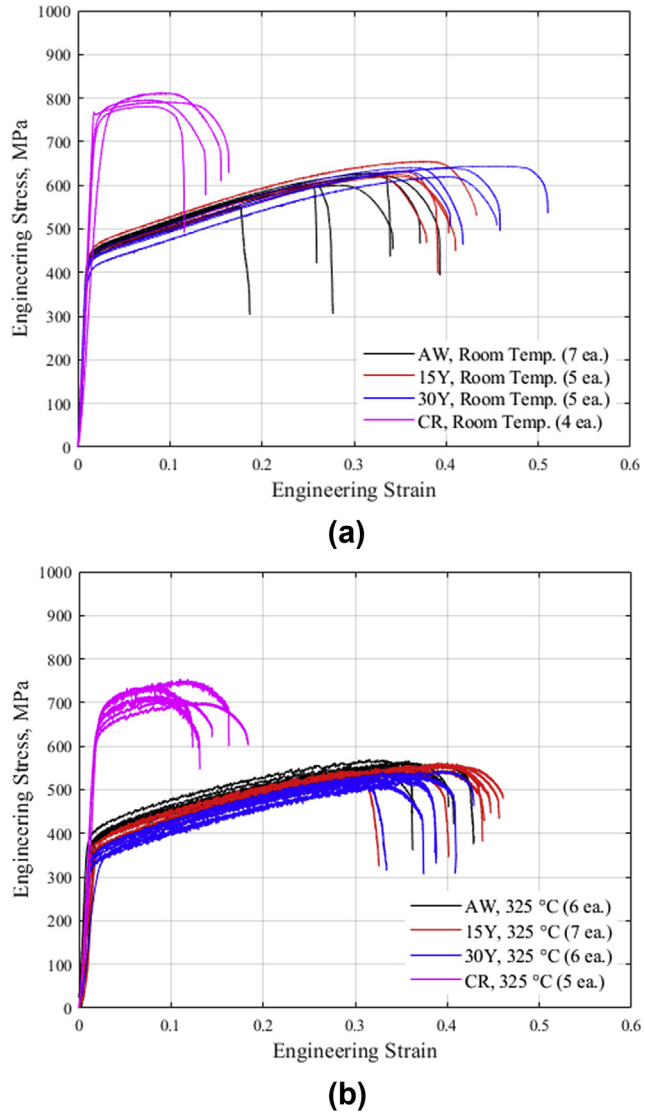

Fig. 8. S–S curves of Alloy 182 weld tensile specimens at (a) RT and (b) 325 °C.

relatively low-stress PWSCC data; however, in this study, the applied stress levels are relatively high [16].

To solve this problem, we performed a two-track approach as follows: 1) the parameters of the Garud model for Alloy 182 were estimated (or calibrated), and 2) a new PWSCC initiation model based on the plastic energy concept was developed.

3.4. Development of probabilistic PWSCC initiation model

Fig. 13 (a) shows the tensile curves of the true stress (σ_{true}) versus the shifted plastic strain ($\varepsilon_{p,\text{shift}}$) at 325 °C using the data in Fig. 8 (b), where the shifting of the plastic strain was carried out in order that all the plastic parts of the S– S curves aligned on a virtual single line (i.e., common flow stress line). The result can be interpreted as the virtual single S– S curve with several unloading and reloading processes. It is widely known that the reloaded S– S curve passes through the point where the previous unloading started [61]. From Fig. 13 (a), regardless of the post-processing condition, it is likely that all the flow stress of Alloy 182 at 325 °C can be described as the shifted plastic strain (or accumulated equivalent plastic strain) that decreased by thermal aging and increased by cold work (see Fig. 7). However, it should be noted that thermal aging also decreased the average true necking stress, especially at 30Y, because of the reduced elongation by the large and incoherent precipitates.

Fig. 13 (b) illustrates the schematic result of Fig. 13 (a) and the assumption that there is a certain threshold stress (σ_{th}) which can be interpreted as a yield stress when the material is perfectly annealed and there is no damage. In Fig. 13 (b), σ_y and σ_u are the true stresses at the start of yielding ($\cong$YS) and necking (or plastic instability), respectively. $\varepsilon_{p,i}$, $\varepsilon_{p,a}$, and $\varepsilon_{p,r}$ are the accumulated equivalent plastic strains at the initial state, generated by the applied loading, and remained until the necking, respectively. Therefore, the areas of (1), (2), and (3) could be interpreted as follows:

- Area of (1): Unrecoverable plastic energy before loading (A_1)
- Area of (2): Unrecoverable plastic energy during loading (A_2)
- Area of (3): Remained plastic energy until plastic instability (A_3)

And here the plastic energy ratio (PER, r_{PE}) is defined as the ratio of the total plastic energy and the unrecoverable plastic energy (see Eq. (5)). The value of r_{PE} was calculated using a trapezoidal approximation as follows:

$$r_{\text{PE}} = \frac{\text{Unrecoverable Plastic Energy}}{\text{Total Plastic Energy until Plastic Instability}} = \frac{A_1 + A_2}{A_1 + A_2 + A_3} \cong \frac{\frac{1}{2}(\varepsilon_{p,i} + \varepsilon_{p,a})(\sigma + \sigma_{\text{th}})}{\frac{1}{2}(\varepsilon_{p,i} + \varepsilon_{p,a} + \varepsilon_{p,r})(\sigma_u + \sigma_{\text{th}})} \cong \frac{(\sigma - \sigma_{\text{th}})(\sigma + \sigma_{\text{th}})}{(\sigma_u - \sigma_{\text{th}})(\sigma_u + \sigma_{\text{th}})} \cong \frac{\sigma^2 - \sigma_{\text{th}}^2}{\sigma_u^2 - \sigma_{\text{th}}^2} \tag{5}$$

based on the microstructural parameters, which are usually hard to estimate and vary with the location of the material. However, the Garud model developed for Alloy 600 cannot be directly applied to this case because this model always predicts prompt PWSCC initiation for every post-processing case based on the given applied stresses [in Fig. 3 (b)] and mechanical properties (in Table 3). This problem appears to be caused by two things: 1) the suggested Garud model parameters were estimated for Alloy 600 and not for Alloy 182, and 2) the original research conducted by Garud used

At this stage, we propose the following empirical power function as a new model of PWSCC initiation time, called the *PER-power model*:

$$t_i \propto (r_{\text{PE}})^{-m} \tag{6}$$

where σ_{th} and m are the model parameters that should be

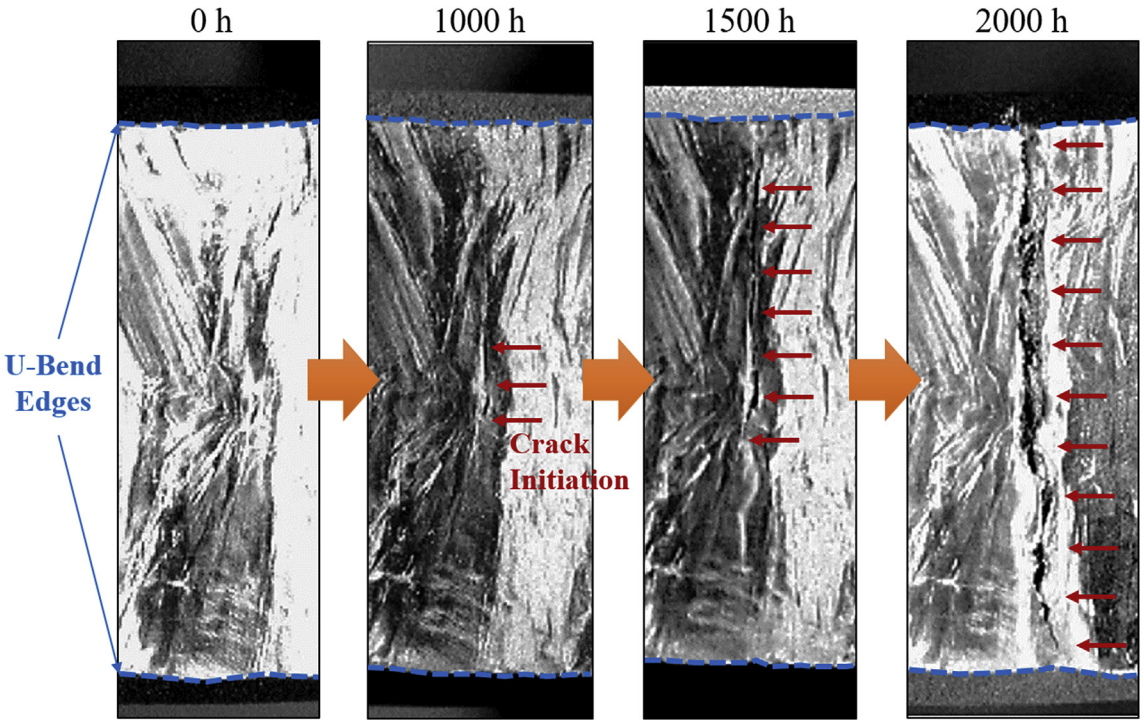

Fig. 9. PWSCC initiation and propagation of #13-AW specimen.

estimated using PWSCC data.

For the estimation, we collected the published Alloy 182 PWSCC initiation data for which the applied stress, YS, and UTS were known. Table 5 describes the information of the collected data [14,15,62–64], and Fig. 14 shows all PWSCC initiation data, including those from this study and the published data in Table 5. The plotted data points of previous reports were extracted through graph digitizing. The effect of different testing temperatures used in the published data (see Table 5) was normalized at 340 °C using the Arrhenius equation with the activation energy of 185 kJ/mol. The U-bend data plotted using the closed symbols in Fig. 14 indicate the observation time of cracking (not the precise cracking time but the upper limit, see Fig. 11). The applied stresses of the U-bend data were assumed to be the highest FEA stresses in Fig. 3 (b). Although this assumption may not be accurate for CR specimens, it is a conservative assumption considering the resulting PWSCC initiation model.

However, as shown in Table 5, there are no reported values of σ_u in the published data. Therefore, we used the following empirical relationship to estimate σ_u from the given YS and UTS data:

$$\sigma_u = \mathrm{UTS_{ET}}(1 + \mathrm{uEL_{ET}}) \tag{7a}$$

where

$$\mathrm{uEL_{ET}} = a_0(\mathrm{UTS_{ET}} - \mathrm{YS_{ET}})^{b_0} + \frac{\mathrm{UTS_{ET}}}{E_{\mathrm{ET}}} \tag{7b}$$

The subscript ET indicates the elevated temperature range under the typical PWR primary water condition (e.g., 325–350 °C); uEL is the uniform (engineering) elongation, and a_0 and b_0 are the material-dependent fitting parameters. In the case of Alloy 182, we estimated the fitting parameters using the tensile test data from this study (Fig. 15). It was observed that the fitting function in Fig. 15 is a good fit for the raw data points. The estimated fitting parameters for Alloy 182 were $a_0 = 7.725 \times 10^{-5}$ MPa^{-1} and $b_0 = 1.570$.

The aforementioned Garud model (Eq. (2)) and the PER-power model (Eq. (6)) are deterministic models. Thus, to consider the censored data, it is necessary to convert the two models from deterministic to probabilistic models. Therefore, we combined the two-parameter Weibull distribution (Eq. (4)) and the aforementioned models as follows:

- Garud model (for Alloy 182)

$$\eta = \lambda \ln(A) \frac{\ln\left(\frac{A-z}{\frac{\sigma}{\mathrm{YS_{RT}}}-z}\right)}{\ln\left(\frac{A-z}{1-z}\right)} \frac{1}{m^q} \tag{8}$$

- PER-power model

$$\eta = \lambda (r_{\mathrm{PE}})^{-m} \tag{9}$$

Here, η and λ are the Weibull scale parameters and the calibration parameters, respectively. In this study, the calibration parameter λ included the effects of temperature, water chemistry, specimen geometry/size, surface finish, criterion of crack initiation, and so on. Therefore, the estimates of λ varied with each data set. We also assumed that the estimates of the Weibull shape parameter β varied with each data set. The objective of the estimation can be summarized as follows:

- Garud model (for Alloy 182): Estimated eleven parameters (β, $\lambda, a, b, c, k, v, w, q, z_1$, and z_2) using the data in Figs. 11 and 14 and Tables 3 and 5, with four input variables ($\sigma, E_{\mathrm{RT}}, \mathrm{YS_{RT}}$, and $\mathrm{UTS_{RT}}$).

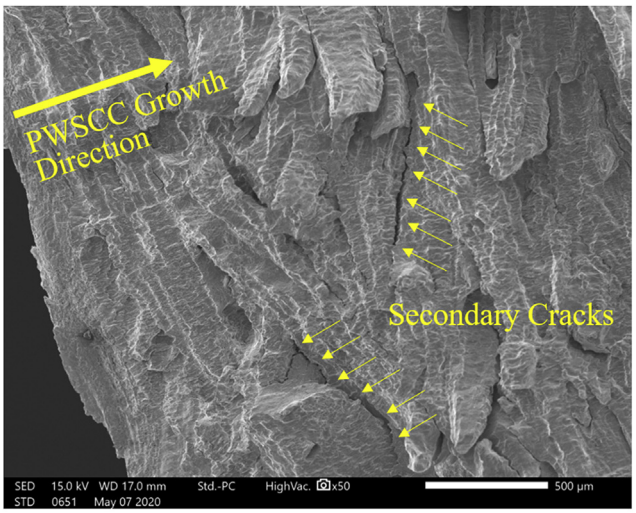

(a)

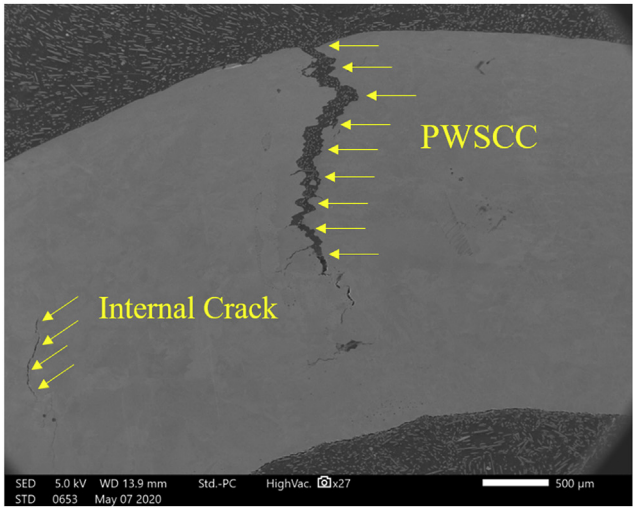

(b)

Fig. 10. Secondary electron SEM images showing PWSCC (a) fracture surface of #39-CR and (b) cross section of #44-CR specimens.

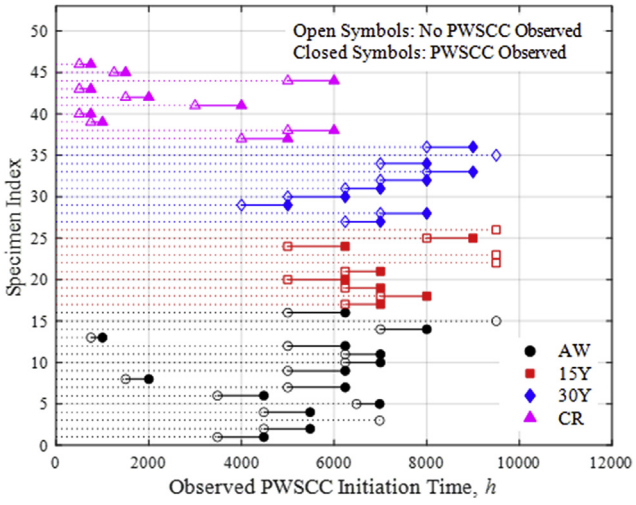

Fig. 11. Results of SCC initiation test with U-bend specimens (corrected at 340 °C).

Table 4
Estimation results of 2-parameter Weibull distribution for SCC initiation time.

Specimen Condition	CR	AW	15Y	30Y
Estimates of Shape Parameter, $\widehat{\beta}$	1.2754	2.5068	4.0817	5.4484
Estimates of Scale Parameter, $\widehat{\eta}$ [h]	2674.8	6282.6	8736.1	7900.8

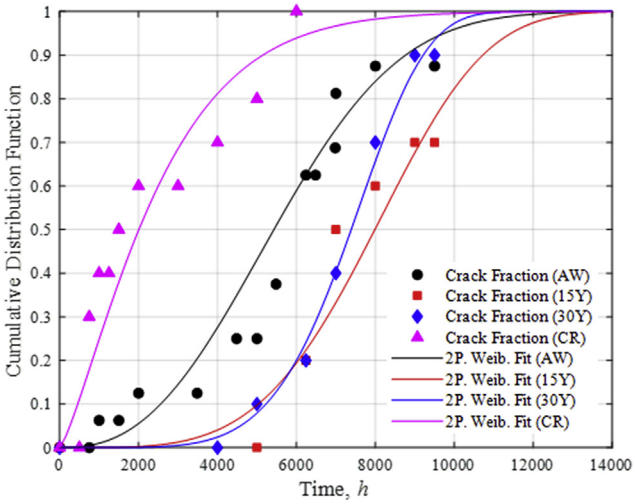

Fig. 12. Cracking fraction and estimated of 2-parameter Weibull distribution for each specimen.

- PER-power model: Estimated four parameters (β, λ, σ_{th}, and m) using the data in Figs. 11 and 14 and Tables 3 and 5 with four input variables (σ, E_{ET}, YS_{ET}, and UTS_{ET}).

This is a probabilistic, nonlinear, and multivariable estimation. To estimate the parameters, we used the MLE method [54–57] again. During the estimation, the elastic moduli at both RT and ET (i.e., E_{RT} and E_{ET}, respectively) were assumed to be 197.2 GPa [65]. However, because the Garud model becomes discontinuous at $\sigma/YS_{RT} = z$, the parameters z_1, z_2 were assumed to be 0.548 and 0.404, respectively; these are parameter values immediately before the divergence of the MLE, but they also return the maximum log-likelihood [53].

Table 6 shows the estimation results of the Garud and PER-power models for Alloy 182. From this table, it is evident that the likelihood of the PER-power model is approximately 2.21×10^{14} ($\cong e^{-490.6+523.6}$) times higher than that of the Garud model. In other words, the PER-power model is considerably more plausible than the Garud model, even though the number of model parameters is lesser (i.e., four vs. eleven). In addition, it is unreasonable that the sign of the estimated Garud parameter w is negative, which implies that the upper limit of stress severity increases when the material is cold worked [16]. This appears to be caused by the two following reasons: 1) the functional form of the Garud model is inherently inappropriate for fitting the Alloy 182 PWSCC initiation data. Therefore, many parameters in the Garud model caused overfitting problem, and 2) inputs to the Garud model are mechanical properties at RT, which are not at the properties at the actual PWSCC testing temperature, ET.

Fig. 16 presents a correlation of the measured PWSCC initiation time and the predicted PWSCC initiation time. As the two models were converted into the probabilistic Weibull distribution, we represented the median of the distribution (i.e., the time at which the probability of cracking was 50%) as the predicted PWSCC initiation time. The black dashed lines in Fig. 16 indicate the shifted

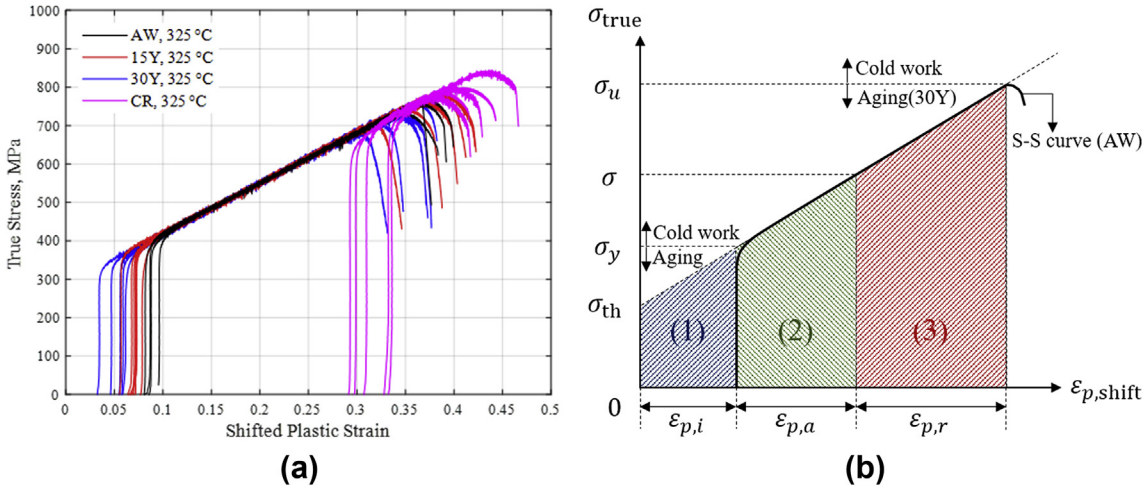

Fig. 13. (a) Alloy 182 tensile curves of true stress versus shifted plastic strain at 325 °C, (b) schematic illustration of (a).

Table 5
Information of published PWSCC initiation data sets of Alloy 182.

Data Reference	YS [MPa]		UTS [MPa]		PWSCC Testing Temperature [°C]	PWSCC Specimen	Number of Data
Couvant [62]	RT	386	RT	627	325–360	Tensile	6 SCC
	350 °C	347	350 °C	568			9 No SCC
Scott [63]	RT	363	RT	637	330–360	Pressurized Capsule	8 SCC
	350 °C	321.7	350 °C	549.3			6 No SCC
Vaillant [14,15,64]	RT	395	RT	657	325	Tensile (Polished)	10 SCC
	350 °C	353	350 °C	584[a]			30 No SCC
						Tensile (Lathed)	18 SCC
							8 No SCC

[a] Estimated from RT data [14].

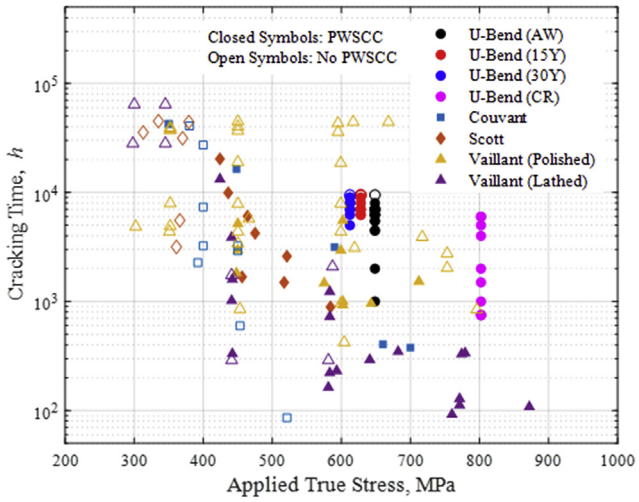

Fig. 14. All Alloy 182 PWSCC initiation data including U-bend and published data in Table 5 (corrected at 340 °C).

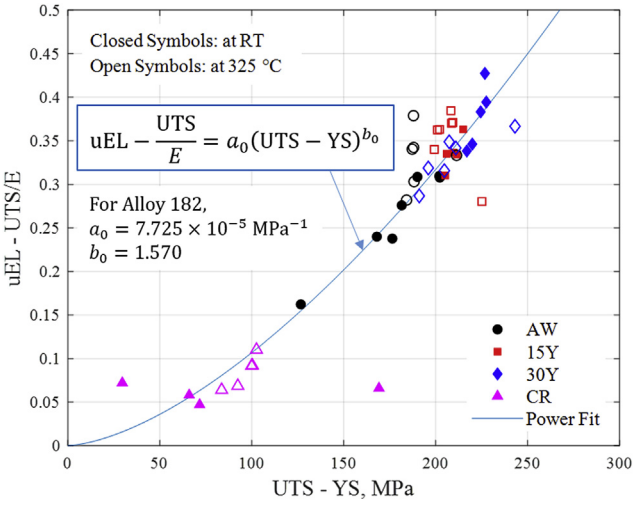

Fig. 15. Estimation result of a_0, b_0 parameter for Alloy 182 using tensile data in Fig. 8.

1:1 prediction lines with a factor of five. When comparing the results, it should be noted that a model becomes more plausible when the NO PWSCC (i.e., censored) data are located as far above as possible from the 1:1 prediction line [see Fig. 16 (c), (d)], contrary to the ordinary PWSCC data [see Fig. 16 (a), (b)]. Therefore, it is shown that the PER-power model is better than the Garud model for the Alloy 182 PWSCC initiation.

Fig. 17 depicts the U-bend PWSCC initiation data plotted with PER, where the solid line indicates the estimated line of 50% cracking probability, and the shaded area indicates the associated 90% confidence interval. It is shown that the PER-power model and its confidence interval naturally fit almost all the U-bend PWSCC initiation data. That is, the effects of thermal aging and cold work can be appropriately modeled using the suggested PER-power model with the mechanical properties at ET. In this model, the

Table 6
Estimation result of Garud and PER-power model for Alloy 182.

Models		Garud Model (Alloy 182)	PER-Power Model
Input Variables		$\sigma, E_{RT}, YS_{RT}, UTS_{RT}$	$\sigma, E_{ET}, YS_{ET}, UTS_{ET}$
Output Variable		$F(t)$	$F(t)$
Log-Likelihood		−523.64	−490.61
Parameters depending on Data Set	U-Bend (All)	$\beta = 2.245$, $\lambda = 21936$ h	$\beta = 2.246$, $\lambda = 3194$ h
	Couvant	$\beta = 1.085$, $\lambda = 27740$ h	$\beta = 1.533$, $\lambda = 326$ h
	Scott	$\beta = 0.880$, $\lambda = 21182$ h	$\beta = 2.851$, $\lambda = 231$ h
	Vaillant (Polished)	$\beta = 0.547$, $\lambda = 19319$ h	$\beta = 0.513$, $\lambda = 8256$ h
	Vaillant (Lathed)	$\beta = 0.632$, $\lambda = 6488$ h	$\beta = 1.219$, $\lambda = 122$ h
Universal Parameters regardless of Data Set		$a = 0.489$	$\sigma_{th} = 298$ MPa
		$b = -1.106$	$m = 2.41$
		$c = 0.0618$	
		$k = 8.161$	
		$v = 2.358$	
		$w = -0.0341$	
		$q = 0.871$	
		$z_1 = 0.548$ (Assumed)	
		$z_2 = 0.404$ (Assumed)	

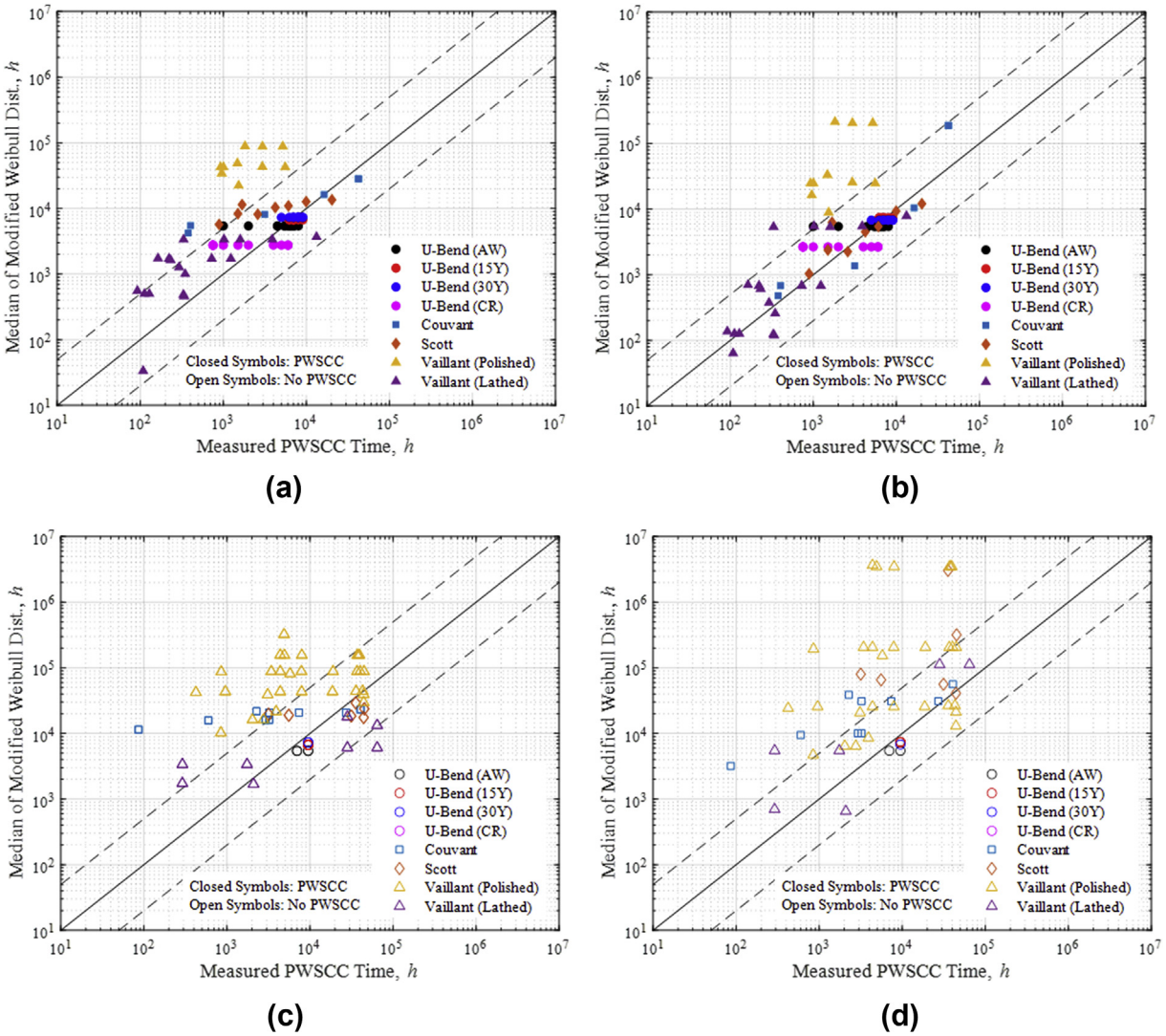

Fig. 16. Correlation of measured PWSCC initiation time versus predicted PWSCC initiation time for Alloy 182: case of PWSCC data for (a) Garud model, (b) PER-power model and case of NO PWSCC data for (c) Garud model, (d) PER-power model.

PWSCC initiation resistance increases as the value of σ_u increases if the applied true stress remains the same. The estimated (average) σ_u obtained using Eq. (7) for the AW, 15Y, 30Y, and CR specimens are 729, 743, 712, and 799 MPa, respectively. Therefore, when the applied true stress remains constant, it is anticipated that the PWSCC resistance of Alloy 182 welds increases at 15Y and decreases

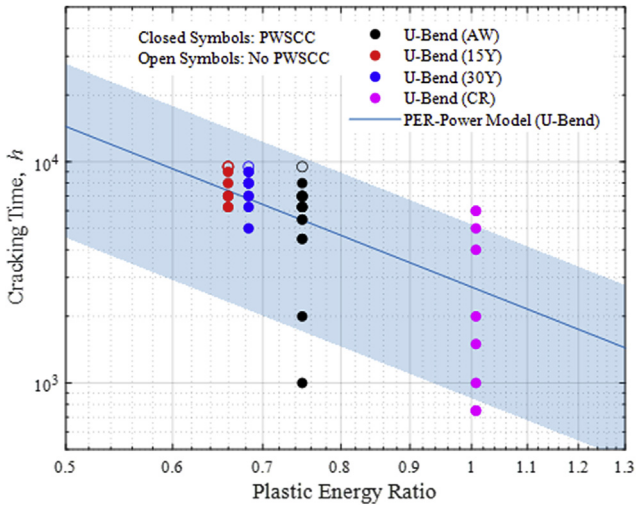

Fig. 17. U-bend PWSCC initiation data plotted with PER.

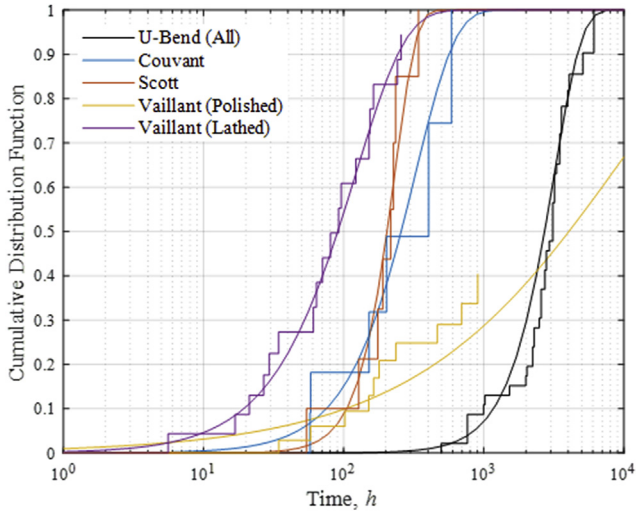

Fig. 18. Comparison of empirical CDF versus Weibull distribution after data normalization at '$r_{PE} = 1$' using PER-power model (stairs: empirical CDF, curves: Weibull CDF).

at 30Y of thermal aging. On the contrary, the effect of cold work on PWSCC resistance is shown to be beneficial if the applied true stress remains the same. However, it should be noted that the PER of the cold-worked material is considerably higher than that of the as-welded material when the applied stress is equal to each YS.

Fig. 18 presents a comparison of the empirical CDF and the Weibull distribution after data normalization at "$r_{PE} = 1$" using the PER-power model. The empirical CDFs were estimated using the Kaplan–Meier method [66] in order to consider censored data. As shown in Fig. 18, the estimated Weibull distribution combined with the PER-power model fits well with the PWSCC initiation data for Alloy 182. Therefore, we concluded that the estimated PER-power model is the most practically optimal model for the PWSCC initiation of Alloy 182 among the suggested empirical models so far. It fits well with the raw data and also considers data censoring and multivariable effects probabilistically and simultaneously. Furthermore, it considers the effects of thermal aging and cold work with the measured mechanical properties at ET. However, it should be noted that the model needs to be further improved to apply it to field components by considering other PWSCC factors: corrosion, stress triaxiality, surface finish, geometry, etc.

4. Conclusion

We experimentally investigated the effects of thermal aging and cold work on the microstructure, mechanical properties, and PWSCC initiation of Alloy 182 welds. Furthermore, we developed a probabilistic PWSCC initiation model for Alloy 182 considering thermal aging and cold work. The following conclusions were drawn based on the results obtained:

- The amount and size of the precipitates along grain boundaries increased with thermal aging. However, there was no noticeable effect of cold work on the precipitate fraction at grain boundaries. Coarsened grain boundary precipitates, formed due to thermal aging, were primarily composed of Cr carbides ($Cr_{23}C_6$ or Cr_7C_3). It is presumably because the amount and diffusion rates of other minor elements (such as Nb and Ti) were relatively low at 400 °C.
- Cold work increased localized residual stresses (or geometrically necessary dislocations), while thermal aging relieved existing residual stresses formed during the welding process.
- At the temperature of PWSCC initiation (i.e., 325 °C), it is likely that the material strength are dominantly affected by *work hardening* mechanism. Meanwhile, it is likely that the growth of precipitates through thermal aging has little effect on the material strength. However, the growth of the intergranular precipitates through thermal aging could reduce the elongation of the material.
- It was observed that the scattering of the PWSCC initiation time increased with the degree of localized residual strains.
- The performance of the calibrated Garud model for Alloy 182 was relatively not good; this was attributed to 1) the inappropriate functional form of the Garud model for fitting Alloy 182 PWSCC initiation data, and 2) the mechanical properties at RT used as inputs for the Garud model.
- Using the PER-power model, it was estimated that the PWSCC resistance of Alloy 182 welds would increase at 15Y and decrease at 30Y of thermal aging, provided the applied true stress remained constant.
- The estimated PER-power model was deemed to be practically the best model for the PWSCC initiation of Alloy 182 among the suggested empirical models so far. This was because it fits well with raw data and considers data censoring and multivariable effects probabilistically and simultaneously. It also considers the effects of thermal aging and cold work with the mechanical properties measured at the testing temperature. However, it should be noted that the model needs to be further improved to apply it to field components by considering other PWSCC factors.

Declaration of competing interest

The authors declare that they have no known competing financial interests or personal relationships that could have appeared to influence the work reported in this paper

Acknowledgement

This work was supported by the Korea Institute of Nuclear Safety (KINS, No. 202000370001) and Nuclear Safety Research Program through the Korea Foundation Of Nuclear Safety (KoFONS) using the financial resource granted by the Nuclear Safety and Security Commission (NSSC) of the Republic of Korea. (No. 1403006). This work was also supported by the "Human Resources Program in Energy Technology" of the Korea Institute of Energy Technology Evaluation and Planning (KETEP), granted financial resource from the Ministry of Trade, Industry & Energy, Republic of Korea. (No.

20184010201660).

Appendix A. Supplementary data

Supplementary data to this article can be found online at https://doi.org/10.1016/j.net.2020.12.005.

References

[1] T.M. Pollock, S. Tin, Nickel-based superalloys for advanced turbine engines: chemistry, microstructure and properties, J. Propul. Power 22 (2006) 361–374.
[2] T.H. Lee, I.S. Hwang, H.D. Kim, J.H. Kim, Techniques for intergranular crack formation and assessment in alloy 600 base and alloy 182 weld metals, Nuclear Engineering and Technology 47 (2015) 102–114.
[3] K. Sieradzki, R.C. Newman, Stress-corrosion cracking, J. Phys. Chem. Solid. 48 (1987) 1101–1113.
[4] P. Scott, M.C. Meunier, Materials Reliability Program: Review of Stress Corrosion Cracking of Alloys 182 and 82 in PWR Primary Water Service, EPRI Palo Alto CA, 2007, 1015427.
[5] W. Lunceford, T. DeWees, P. Scott, EPRI Materials Degradation Matrix, vol. 3, EPRI, Palo Alto, CA, USA 3002000628, 2013.
[6] G.A. White, N.S. Nordmann, J. Hickling, C.D. Harrington, Development of Crack Growth Rate Disposition Curves for Primary Water Stress Corrosion Cracking (PWSCC) of Alloy 82, 182, and 132 Weldments, TMS (The Minerals, Metals and Materials Society, 2005.
[7] P. Scott, M.C. Meunier, O. Calonne, M.P. Foucault, P. Combrade, C. Amzallag, Comparison of Laboratory and Field Experience of PWSCC in Alloy 182 Weld Metal, in: Proceedings of the 13th International Conference Environment Degradation of Materials in Nuclear Power Systems-Water Reactors, CDROM, 2007.
[8] Y.S. Lim, S.S. Hwang, S.W. Kim, H.P. Kim, Primary water stress corrosion cracking behavior of an Alloy 600/182 weld, Corrosion Sci. 100 (2015) 12–22.
[9] C. Amzallag, J.-M. Boursier, C. Pages, C. Gimond, Stress Corrosion Life Assessment of 182 and 82 Welds Used in PWR Components, in: 10th International Conference Environmental Degradation of Materials in Nuclear Power Systems—Water Reactors, 2002.
[10] D.O. Harris, D.D. Dedhia, S.C. Lu, Theoretical and Users Manual for Pc-PRAISE: A Probabilistic Fracture Mechanics Computer Code for Piping Reliability Analysis, Nuclear Regulatory Commission, United States). Div. of, Washington, DC, 1992.
[11] P. Scott, R. Kurth, A. Cox, R. Olson, D. Rudland, Development of the PRO-LOCA probabilistic fracture mechanics code, MERIT final report, SSM Report 46 (2010).
[12] M. Erickson, F. Ammirato, B. Brust, D. Dedhia, E. Focht, M. Kirk, C. Lange, R. Olsen, P. Scott, D. Shim, Models and Inputs Selected for Use in the xLPR Pilot Study, Electric Power Research Institute (EPRI), Palo Alto, CA, USA, 2011.
[13] D. Rudland, C. Harrington, R. Dingreville, Development of the extremely low probability of rupture (xLPR) Version 2.0 code. Pressure Vessels and Piping Conference, American Society of Mechanical Engineers, 2015. V06BT06A050.
[14] G. Troyer, S. Fyfitch, K. Schmitt, G. White, C. Harrington, Dissimilar Metal Weld PWSCC Initiation Model Refinement for xLPR Part I: a Survey of Alloy 82/182/132 Crack Initiation Literature, in: Proceedings of the 17th International Conference on Environmental Degradation of Materials in Nuclear Power Systems—Water Reactors, Canada, Ottawa, ON, 2015, pp. 9–13.
[15] F. Vaillant, J.-M. Boursier, C. Amzallag, C. Bibollet, S. Pons, Environmental behaviour and weldability of Ni-base weld metals in PWRs, Rev. Gen. Nucleaire (2007) 62–71.
[16] Y.S. Garud, Stress Corrosion Cracking Initiation Model for Stainless Steel and Nickel Alloys, Electric Power Research Institute (EPRI), Palo Alto, CA, USA, 2009.
[17] Y.S. Garud, R.S. Pathania, A Simplified Model for SCC Initiation Susceptibility in Alloy 600, with the Influence of Cold Work Layer and Strength Characteristics, in: Ninth International Symposium on Environmental Degradation of Materials in Nuclear Power Systems—Water Reactors, Wiley Online Library, 1999, pp. 261–268.
[18] R. Konings, Comprehensive Nuclear Materials, Elsevier, 2011.
[19] J.W. Martin, Precipitation Hardening: Theory and Applications, Butterworth-Heinemann, 2012.
[20] S.C. Yoo, K.J. Choi, T. Kim, S.H. Kim, J.Y. Kim, J.H. Kim, Microstructural evolution and stress-corrosion-cracking behavior of thermally aged Ni-Cr-Fe alloy, Corrosion Sci. 111 (2016) 39–51.
[21] J.J. Kai, G.P. Yu, C.H. Tsai, M.N. Liu, S.C. Yao, The effects of heat treatment on the chromium depletion, precipitate evolution, and corrosion resistance of INCONEL alloy 690, Metal. Trans. A 20 (1989) 2057–2067.
[22] R. Celin, F. Tehovnik, Degradation of a Ni-Cr-Fe alloy in a pressurised-water nuclear power plant, Mater. Technol. 45 (2011) 151–157.
[23] K.J. Choi, J.J. Kim, B.H. Lee, C.B. Bahn, J.H. Kim, Effects of thermal aging on microstructures of low alloy steel–Ni base alloy dissimilar metal weld interfaces, J. Nucl. Mater. 441 (2013) 493–502.
[24] S.C. Yoo, K.J. Choi, C.B. Bahn, S.H. Kim, J.Y. Kim, J.H. Kim, Effects of thermal aging on the microstructure of Type-II boundaries in dissimilar metal weld joints, J. Nucl. Mater. 459 (2015) 5–12.
[25] S.A. Tukur, M.S. Dambatta, A. Ahmed, N.M. Mu'az, Effect of heat treatment temperature on mechanical properties of the AISI 304 stainless steel, Intl J Innov Res Sci, Eng Technol. 3 (2014) 9516–9520.
[26] J.-Y. Jeon, Y.-J. Kim, J.-S. Kim, Computational simulation of cold work effect on PWSCC growth in Alloy 600TT steam generator, J. Mech. Sci. Technol. 30 (2016) 689–696.
[27] T. Maeguchi, K. Sakima, K. Sato, K. Fujimoto, Y. Nagoshi, K. Tsutsumi, PWSCC Susceptibility of Alloy 690, 52 and 152, in: Proceedings of the 18th International Conference on Environmental Degradation of Materials in Nuclear Power Systems—Water Reactors, Springer, 2019, pp. 485–500.
[28] M. Toloczko, Z. Zhai, S. Bruemmer, SCC Initiation Behavior of Alloy 182 in PWR Primary Water, in: Proceedings of the 18th International Conference on Environmental Degradation of Materials in Nuclear Power Systems—Water Reactors, Springer, 2019, pp. 137–160.
[29] T. Shoji, Z. Lu, H. Murakami, Formulating stress corrosion cracking growth rates by combination of crack tip mechanics and crack tip oxidation kinetics, Corrosion Sci. 52 (2010) 769–779.
[30] D.D. Pruthi, M.S. Anand, R.P. Agarwala, Diffusion of chromium in inconel-600, J. Nucl. Mater. 64 (1977) 206–210.
[31] P. Scott, Experimental Program on the Effects of Surface Condition on Primary Water Stress Corrosion Cracking of Alloy 182 Welds, 2007.
[32] ASTM, Standard Practice for Microetching Metals and Alloys, 2015. E407-07.
[33] F. Bachmann, R. Hielscher, H. Schaeben, Texture Analysis with MTEX–free and Open Source Software Toolbox, in: Solid State Phenomena, Trans Tech Publ, 2010, pp. 63–68.
[34] ASTM, ASTM E8/E8M-16a, Standard Test Methods for Tension Testing of Metallic Materials, ASTM International, West Conshohocken, PA, USA, 2016.
[35] ASTM, Standard, Standard Practice for Making and Using U-Bend Stress-Corrosion Test Specimens, 2009. ASTM G30-90.
[36] D. Systemes, Abaqus 2016 User's Manual, 2016.
[37] Special Metals, INCONEL alloy 600, accessed June 20, https://www.specialmetals.com/assets/smc/documents/alloys/inconel/inconel-alloy-600.pdf, 2020.
[38] R.D. Grampurohit, H. Prasanna, IDENTIFICATION OF DISLOCATIONS, GRAIN BOUNDARY SLIDING AND POINT DEFECTS WITH THE AID OF SEM ANALYSIS, 2017.
[39] C.T. Rueden, J. Schindelin, M.C. Hiner, B.E. DeZonia, A.E. Walter, E.T. Arena, K.W. Eliceiri, ImageJ2: ImageJ for the next generation of scientific image data, BMC Bioinf. 18 (2017) 529.
[40] G. Bao, M. Yamamoto, K. Shinozaki, Precipitation and Cr depletion profiles of Inconel 182 during heat treatments and laser surface melting, J. Mater. Process. Technol. 209 (2009) 416–425.
[41] X.-J. Di, X.-Q. Liu, C.-X. Chen, B.-S. Wang, X.-J. Guo, Effect of post-weld heat treatment on the microstructure and corrosion resistance of deposited metal of a high-chromium nickel-based alloy, Acta Metall. Sin. 29 (2016) 1136–1143.
[42] Y.S. Lim, H.P. Kim, H.D. Cho, H.H. Lee, Microscopic examination of an Alloy 600/182 weld, Mater. Char. 60 (2009) 1496–1506.
[43] R.A. Page, Stress corrosion cracking of Alloys 600 and 690 and Nos. 82 and 182 weld metals in high temperature water, Corrosion 39 (1983) 409–421.
[44] Q.J. Peng, H. Yamauchi, T. Shoji, Investigation of dendrite-boundary microchemistry in alloy 182 using auger electron spectroscopy analysis, Metall. Mater. Trans. 34 (2003) 1891–1899.
[45] Q. Peng, J. Hou, Y. Takeda, T. Shoji, Effect of chemical composition on grain boundary microchemistry and stress corrosion cracking in Alloy 182, Corrosion Sci. 67 (2013) 91–99.
[46] Y. Sakakibara, K. Kubushiro, Stress evaluation at the maximum strained state by EBSD and several residual stress measurements for plastic deformed austenitic stainless steel, World J. Mech. 7 (2017) 195–210.
[47] MTEX, (n.d EBSD-Denoising. https://mtex-toolbox.github.io/EBSDDenoising.html. (Accessed 13 May 2020).
[48] F. Roters, P. Eisenlohr, T.R. Bieler, D. Raabe, Crystal Plasticity Finite Element Methods: in Materials Science and Engineering, John Wiley & Sons, 2011.
[49] T.H. Lee, Y.J. Lee, S.H. Joo, H.H. Nersisyan, K.T. Park, J.H. Lee, Intergranular M23C6 carbide precipitation behavior and its effect on mechanical properties of Inconel 690 tubes, Metall. Mater. Trans.: Physical Metallurgy and Materials Science 46 (2015) 4020–4026, https://doi.org/10.1007/s11661-015-3003-4.
[50] L.E. Thomas, M.J. Olszta, B.R. Johnson, S.M. Bruemmer, Microstructural Characterization of Primary Water Stress-Corrosion Cracks in Alloy 182 Welds from PWR Components and Laboratory Tests, in: The 14th International Conference on Environmental Degradation of Materials in Nuclear Power Systems-Water Reactors, Virginia Beach, 2009.
[51] H. Xu, S. Fyfitch, J.W. Hyres, Laboratory Investigation of PWSCC of CRDM Nozzle 3 and its J-Groove Weld on the Davis-Besse Reactor Vessel Head, in: T.R. Allen, P.J. King, L. Nelson (Eds.), Proceedings of the 12th International Conference on Environmental Degradation of Materials in Nuclear Systems—Water Reactors, TMS, Pittsburgh, PA, 2005, pp. 833–842.
[52] W. Weibull, Wide applicability, J. Appl. Mech. 103 (1951) 293–297.
[53] J.I. McCool, Using the Weibull Distribution: Reliability, Modeling, and Inference, John Wiley & Sons, 2012.
[54] J.P. Park, C. Park, J. Cho, C.B. Bahn, Effects of cracking test conditions on estimation uncertainty for weibull parameters considering time-dependent censoring interval, Materials 10 (2017), https://doi.org/10.3390/ma10010003.
[55] J.P. Park, C.B. Bahn, Uncertainty evaluation of weibull estimators through

Monte Carlo simulation: applications for crack initiation testing, Materials 9 (2016), https://doi.org/10.3390/ma9070521.
[56] J.P. Park, C. Park, Y.-J. Oh, J.H. Kim, C.B. Bahn, Statistical analysis of parameter estimation of a probabilistic crack initiation model for Alloy 182 weld considering right-censored data and the covariate effect, Nuclear Engineering and Technology (2018) 50, https://doi.org/10.1016/j.net.2017.09.005.
[57] J.P. Park, S. Mohanty, C.B. Bahn, S. Majumdar, K. Natesan, Weibull and bootstrap-based data-analytics framework for fatigue life prognosis of the pressurized water nuclear reactor component under harsh reactor coolant environment, Journal of Nondestructive Evaluation, Diagnostics and Prognostics of Engineering Systems 3 (2020).
[58] S.S. Rao, Engineering Optimization: Theory and Practice, John Wiley & Sons, 2019.
[59] Ian de Curieres, Corrosion Issues in Future Years: A Tso Perspective, in: 19th Environmental Degradation of Materials in Nuclear Power Systems – Water Reactors, Boston, 2019.
[60] E. Chaumun, J. Crépin, C. Duhamel, C. Guerre, E. Héripré, M. Sennour, I. de Curières, Stress Corrosion Cracking Initiation of Alloy 82 in Hydrogenated Steam, in: Proceedings of the 18th International Conference on Environmental Degradation of Materials in Nuclear Power Systems–Water Reactors, Springer, 2019, pp. 175–189.
[61] J. Chakrabarty, Applied Plasticity, Springer, 2010.
[62] T. Couvant, F. Vaillant, Initiation of PWSCC of Weld Alloy 182, in: Proceedings of the 15th International Conference on Environmental Degradation of Materials in Nuclear Power Systems—Water Reactors, Springer, 2011, pp. 1141–1154.
[63] P. Scott, M. Foucault, B. Brugier, J. Hickling, A. McIlree, L. Nelson TMS, Examination of Stress Corrosion Cracks in Alloy 182 Weld Metal after Exposure to PWR Primary Water, in: T.R. Allen, P.J. King (Eds.), Proceedings of the 12th International Conference on Environmental Degradation of Materials in Nuclear Power System–Water Reactors–, The Minerals, Metals & Materials Society, 2005, pp. 497–509.
[64] F. Vaillant, J.-M. Boursier, T. Couvant, C. Amzallag, J. Champredonde, Influence of a Cyclic Loading on the Initiation and Propagation of PWSCC in Weld Metal 182, in: 12th Int. Conf. On Environmental Degradation of Materials in Nuclear Power Systems-Water Reactors, Snowbird, UA, 2005, pp. 14–18.
[65] J.-D. Hong, C. Jang, T.S. Kim, PFM application for the PWSCC integrity of Ni-base alloy welds—development and application of PINEP-PWSCC, Nucl. Eng. Technol. 44 (2012) e970.
[66] E.L. Kaplan, P. Meier, Nonparametric estimation from incomplete observations, J. Am. Stat. Assoc. 53 (1958) 457–481.